NANO LETTERS
Letter
Cite This: Nano Lett. 2020, 20, 502−508
pubs.acs.org/NanoLett

High Broadband Light Transmission for Solar Fuels Production Using Dielectric Optical Waveguides in TiO_2 Nanocone Arrays

Sisir Yalamanchili,[†,#] Erik Verlage,[†,#] Wen-Hui Cheng,[†,#] Katherine T. Fountaine,[⊥] Philip R. Jahelka,[†] Paul A. Kempler,[‡] Rebecca Saive,[†] Nathan S. Lewis,[*,‡,∥] and Harry A. Atwater[*,†,§]

[†]Division of Engineering and Applied Sciences, [‡]Division of Chemistry and Chemical Engineering, [§]Kavli Nanoscience Institute, and [∥]Beckman Institute, California Institute of Technology, Pasadena, California 91125, United States

[⊥]NGNext, Northrop Grumman Aerospace Systems, Redondo Beach, California 90278, United States

Supporting Information

ABSTRACT: We describe the fabrication and use of arrays of TiO_2 nanocones to yield high optical transmission into semiconductor photoelectrodes covered with high surface loadings of light-absorbing electrocatalysts. Covering over 50% of the surface of a light absorber with an array of high-refractive-index TiO_2 nanocones imparted antireflective behavior (<5% reflectance) to the surface and allowed >85% transmission of broadband light to the underlying Si, even when thick metal contacts or opaque catalyst coatings were deposited on areas of the light-facing surface that were not directly beneath a nanocone. Three-dimensional full-field electromagnetic simulations for the 400−1100 nm spectral range showed that incident broadband illumination couples to multiple waveguide modes in the TiO_2 nanocones, reducing interactions of the light with the metal layer. A proof-of-concept experimental demonstration of light-driven water oxidation was performed using a p^+n-Si photoanode decorated with an array of TiO_2 nanocones additionally having a Ni catalyst layer electrodeposited onto the areas of the p^+n-Si surface left uncovered by the TiO_2 nanocones. This photoanode produced a light-limited photocurrent density of ∼28 mA cm^{-2} under 100 mW cm^{-2} of simulated air mass 1.5 illumination, equivalent to the photocurrent density expected for a bare planar Si surface even though 54% of the front surface of the Si was covered by an ∼70 nm thick Ni metal layer.

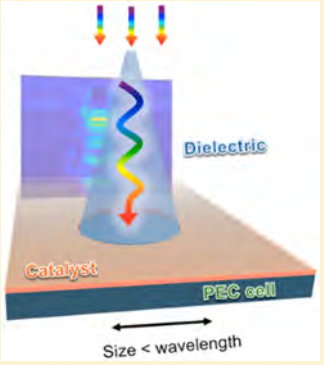

KEYWORDS: *Dielectric nanocone, broadband transmission, nanophotonic, optoelectronic, photoelectrochemical, photovoltaic*

High efficiency conversion of solar energy to electricity or fuels using photovoltaic (PV)[1−5] or photoelectrochemical (PEC)[6−8] cells requires optimization of the broadband absorption of sunlight. Antireflective coatings (ARCs),[9] surface textures,[10−13] and high-index light-trapping structures[14,15] are among the many strategies that have been shown to increase broadband absorption relative to unmodified planar light absorbers. PECs and multijunction PVs generally require front contacts and/or electrocatalytic films that substantially reflect or absorb light, thereby reducing their photocurrent densities.[16] In integrated PECs used to effect solar-driven water splitting or CO_2 reduction,[17−19] the front contact is made to an electrolyte, and a catalyst located in the optical path increases the efficiency of the cell by reducing the kinetic barrier for the electrochemical half-reaction occurring at the top contact. Depending on the orientation of the design, as well as the chemical inputs and desired products, the catalyst may be optically opaque (such as CoP for water reduction or Cu for CO_2 reduction) or may be electrochromic (such as $NiFeO_x$ for water oxidation).[20] Although an all-back-contact design[21,22] can prevent contact shading losses in crystalline Si solar cells, such a design is not compatible with all of the solid/liquid interfaces either with integrated PECs for highly efficient fuel production or with multijunction PV device structures.[23]

Nanostructuring the semiconductor is one approach that has been developed to enhance broadband absorption. Nanowires,[24−26] inverted pyramids,[27] nanodomes,[28] nanoshells,[29] nanopillars,[30,31] and nanocones[32] have been explored for use in many optoelectronic devices. For example, for wavelengths ranging between 400−1100 nm and angles-of-incidence between 0° − 50°, Si microcone arrays exhibit nearly perfect angularly and spectrally averaged reflectivity (<1%) as well as high (89.1%) absorption.[33] Sparse arrays of InP nanocones also exhibit angle-insensitive, near-unity (>90%), broadband (450−900 nm) optical absorption.[34] Cones inherently possess a continuous range of radii that provides a range of waveguide modes accessible for coupling with incident light.[35] Hence, cones are intrinsically favorable structures for enabling enhanced broadband absorption. Moreover, the radius at the base of the cone and the radius of any truncation can be chosen specifically to select a spectral range of interest.

Alternatively, broadband absorption can be enhanced by decorating the light-facing surface of the semiconductor with dielectric nanostructures, such as nanospheres,[36] that serve as

Received: October 12, 2019
Revised: November 29, 2019
Published: December 10, 2019

DOI: 10.1021/acs.nanolett.9b04225
Nano Lett. 2020, 20, 502−508

waveguides. This approach requires a high-index dielectric that can be deposited on planar surfaces using scalable methods. For integrated PEC devices, the dielectric also must be stable in the chosen aqueous electrochemical environment. TiO_2 has been used in waveguides for near-visible and telecommunication wavelengths[37−42] and has a higher index of refraction ($n \sim 2.5$) than many other dielectric materials commonly used in solar photovoltaic devices, including SiO_2 ($n = 1.5$) and Al_2O_3 ($n = 1.77$). TiO_2 is relatively inert electrochemically and has a wide band gap that allows transmission of incident solar illumination, and has been utilized extensively as a protective coating in efficient PEC devices.[17−19,43−48] TiO_2 is therefore a promising candidate material for nanostructured waveguides in PEC devices.

Devices that make use of nanostructured surfaces nevertheless require front contacts, either to a conductor for PVs or to a catalyst for PECs, but the front contact can block light. In devices that require connections between external circuits and nanostructured optical surfaces, front contacts typically are formed by coating the surface with a transparent and conductive material, such as indium tin oxide (ITO). However, efficient integrated PECs for fuel production additionally require catalysts on at least one of the optical surfaces. Very high (>90%) absorption and high front-surface conductivity have been demonstrated using both simulation and experiment in a device consisting of SiN_x-coated Si nanopillars protruding from a crystalline Si substrate coated with an opaque Au front-side contact that covered 65% of the Si surface.[31] Although the selective etching process used in this approach limits its applicability to a few specific interfaces such as Au/Si, this work shows that nanostructures can direct light around opaque metallic front contacts deposited onto the optical surfaces of PV devices and suggests a strategy for guiding light around catalyst layers in PECs.

Considered together, the prior work in the areas of antireflective nanostructures and dielectric waveguides underscores the potential value and developmental feasibility of modular antireflective coatings that promote broadband absorption over a spectral range above the photoelectrode bandgap without requiring modification of the underlying semiconductor or contact interfaces. Herein, we combine simulations and proof-of-concept experiments to evaluate and demonstrate light management by an array of TiO_2 nanocones placed on the surface of a p^+n-Si photoanode with a metallic Ni contact covering the exposed Si surface.

Figure 1 shows schematics for three device configurations that were compared using simulations, to understand the optical properties of TiO_2 nanocones. In the first configuration (Figure 1a), TiO_2 nanocones with a height of 2300 nm and a base radius of 250 nm were placed on the Si substrate in a two-dimensional hexagonal array with a 700 nm pitch. This arrangement left 54% of the Si surface uncovered by TiO_2 nanocones. In the second configuration (Figure 1b), 50 nm of Ni covered the area of Si that remained exposed in the first configuration. The third configuration (Figure 1c) was the same as the second, but the TiO_2 nanocones were removed, leaving a hexagonal array of circles of exposed Si in the Ni layer.

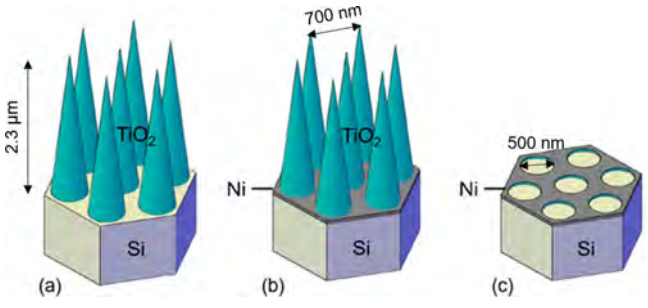

Figure 1. Schematics of the three configurations that were simulated. (a) TiO_2 nanocones on Si substrate; (b) Ni between the TiO_2 nanocones on Si substrate; (c) Ni hole arrays on Si substrate.

Figure 2 compares the simulated transmission, absorption, and reflection spectra for the TiO_2 and Ni components of the three structures, either in air ($n = 1.0$) or in water ($n = 1.33$). Figure 2a,d shows that the TiO_2 nanocones neither absorb nor reflect substantially in the 400−1100 nm spectral range with the nanocones allowing transmission of 97.5% of the total incident photons in air or 96.9% in water. The planar TiO_2 film simulations with higher reflection losses, are shown in Figure S1, leading to transmission of 74.7% in air and 84% in water. When 50 nm of Ni was added into the spaces between the nanocones, the simulated transmitted photon flux was reduced to 86.2% in air or 84.7% in water (Figure 2b,e). The minima in transmission primarily result from absorption by Ni, and the wavelengths of the minima shift depending on the index of refraction of the surrounding environment.

When the TiO_2 nanocones were removed from the simulation, leaving just the hexagonal array of circular holes in a 50 nm layer of Ni that covered 54% of the optical plane, the transmitted photon fluxes were reduced to 23.3% in air or 24.8% in water with reflection and parasitic absorption accounting for ≥75% of the optical losses (Figure 2c,f). The size and pitch of the holes in the Ni layer were particularly unfavorable for transmission of light through the Ni layer in the absence of the TiO_2 cones, because over a large fraction of the incident solar spectrum the diameter of the holes was less than the wavelength of the incident light. In the specific configuration shown in Figure 1b, the TiO_2 nanocones minimized the interaction between the light and the Ni layer, enabling >3 times the amount of light to be transmitted than for the Ni hole array that did not also contain the TiO_2 cones. For the TiO_2 nanocone array with Ni, the simulated transmission at the minima was ≥60%, Figure 2b,e, whereas for the Ni hole array without TiO_2 nanocones, the simulated transmission was 20−30%, Figure 2c,f. The simulations thus indicated that incident light is expected to couple efficiently to the TiO_2 nanocones that guide the light around the Ni layer.

Figure S2 plots the transmitted photon flux for each structure along with the air mass (AM) 1.5G solar spectrum. Using the transmitted spectral photon flux, the maximum photocurrent densities, $J_{ph,max}$, in air estimated from the simulations for a Si solar cell covered by either the TiO_2 nanocone array, the TiO_2 nanocone array with Ni, or the Ni hole array were $J_{ph,max}$ = 42.9, 37.9, and 10.9 mA cm^{-2}, respectively. In water, the corresponding estimated simulated maximum photocurrent densities were $J_{ph,max}$ = 41.8, 36.5, and 10.7 mA cm^{-2}, respectively.

Figure 3 shows the simulated profiles of the electric field along the central cross section of a nanocone. Figure 3c−f shows the field profiles for wavelengths of 484, 552, 628, and 770 nm, respectively, which correspond to the maxima in the transmission spectra shown in Figure 2b. The electric field was predominantly confined to the waveguide modes in the nanocone with strong coupling of incident light occurring at

DOI: 10.1021/acs.nanolett.9b04225
Nano Lett. 2020, 20, 502−508

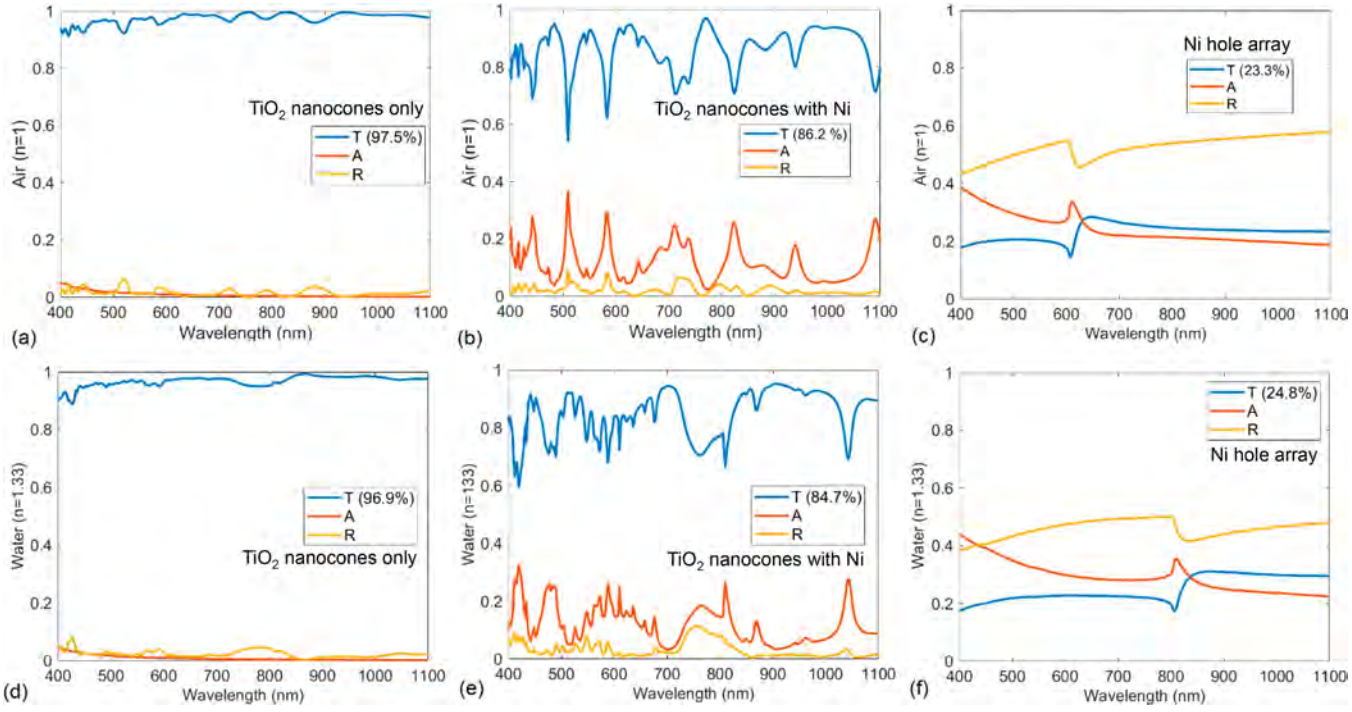

Figure 2. Simulated transmission (T), absorption (A), and reflection (R) spectra of the three configurations of the TiO_2 nanocone array and Ni layer in Figure 1. (a–c) Plot of the spectra in air for an array of TiO_2 cones, a TiO_2 cone array with Ni, and a Ni hole array, respectively. (d–f) Plot of the same structures but in water. The optical effects of the Si substrate are not shown.

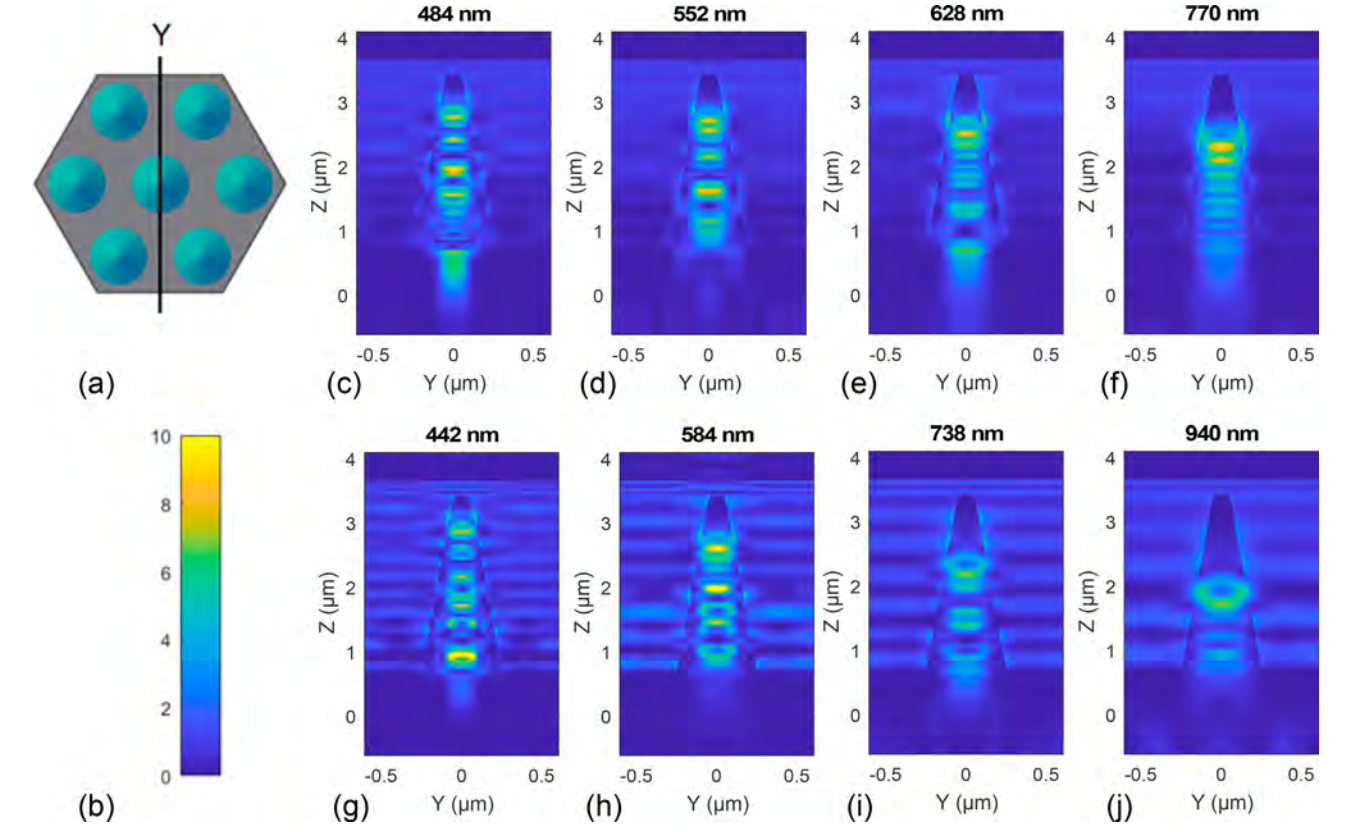

Figure 3. Simulated electric field profiles along the cross section of a TiO_2 nanocone on a Si substrate. (a) Cross section and (b) scale for the relative electric field intensity for the profile plots. (c–f) Profiles for wavelengths of 484, 552, 628, and 770 nm, respectively, which correspond to the maxima in the transmission spectra shown in Figure 2b. (g–j) Profiles for wavelengths of 442, 584, 738, and 940 nm, respectively, which correspond to minima in the transmission spectrum in Figure 2b.

DOI: 10.1021/acs.nanolett.9b04225
Nano Lett. 2020, 20, 502–508

different radii for the different wavelengths, as expected for a conical nanostructure.[33−35] In the simulation, the light propagated through the nanocone and was transmitted into the Si substrate, where the field intensity decreased due to absorption by the Si. Figure 3g−j shows the field profiles for wavelengths of 442, 584, 738, and 940 nm, respectively, which correspond to the minima in the transmission spectra shown in Figure 2b. Compared to the field profiles shown in Figure 3c−f, the profiles in Figure 3g−j showed an increased intensity of the electric field in the space adjacent to the nanocone. The corresponding plots for transmitted light intensities $|E|^2$ versus Y (μm) at the interfaces of Si/Ni (indicated as on Si) and Ni/air (indicated as on Ni) are shown in Figure S3.

Depending on the dimensions of the nanocones and the background index of refraction, simulations indicated that the electric fields associated with some wavelengths of light were highly confined inside the TiO_2 nanocone, whereas the electric fields associated with other wavelengths were only partially confined. Simulation results with varying dimensions of cones are presented in Figure S4. In contrast, the optical absorption in the Ni was enhanced for the wavelengths of light that were not completely confined within the nanocones. The wavelength-dependent variation in the confinement of the electric field within TiO_2 nanocones cannot be explained using effective medium theory. Instead, wave-optic simulations showed that the nanocones acted as antennae for the incoming radiation, coupling the light to waveguide modes, and providing a route for the light to reach the underlying Si substrate even though 54% of the surface was covered by Ni.

The optimal structures revealed by simulation were fabricated and investigated in detail. To experimentally demonstrate the enhancement in photocurrent density obtainable by utilizing TiO_2 nanocone arrays, planar p^+n Si homojunction photoanodes were prepared by doping n-type Si with boron (B). Briefly, electron-beam evaporation was used to deposit 5−10 nm of SiO_2 over the Si photoanodes, prior to deposition of 2.3 μm of TiO_2. Electron-beam evaporation depletes the TiO_2 source of oxygen and thus increases the conductivity of the resulting films, so the 5−10 nm thick SiO_2 was deliberately incorporated to electrically isolate the TiO_2 from making an electrical contact to the highly doped p^+-Si surface, while minimally affecting the optical behavior. The refractive index n, k of TiO_2 was characterized using ellipsometry (J.A. Woollam Co. model VASE). Electron-beam lithography was used to pattern spin-coated poly(methyl methacrylate) (PMMA) with a hexagonal array of 100 nm diameter circular holes with a 700 nm pitch. Two hundred nanometers of Cr was evaporated onto these samples, followed by liftoff, resulting in a hexagonal array of Cr circles that was used as an etching mask. An SF_6/C_4F_8 etching recipe was developed to fabricate TiO_2 nanocones by inductively coupled plasma reactive-ion etching (ICP-RIE). These samples were made into electrodes and Ni was electrodeposited between the TiO_2 nanocones until ~300 mC cm^{-2} of cathodic charge had been passed. Charge normalization to the exposed Si area between nanocones indicated an equivalent of an ~70 nm thick flat Ni layer, which is slightly higher than the 50 nm value used in the simulations. Experimental details are included in Supporting Information, and an illustration of the process flow for fabrication of the desired structures is shown in Figure S5.

Figure 4 shows scanning-electron micrographs (SEMs), before and after electrodeposition of Ni, for samples of dry-etched TiO_2 nancone arrays on planar p^+n-Si substrates. The

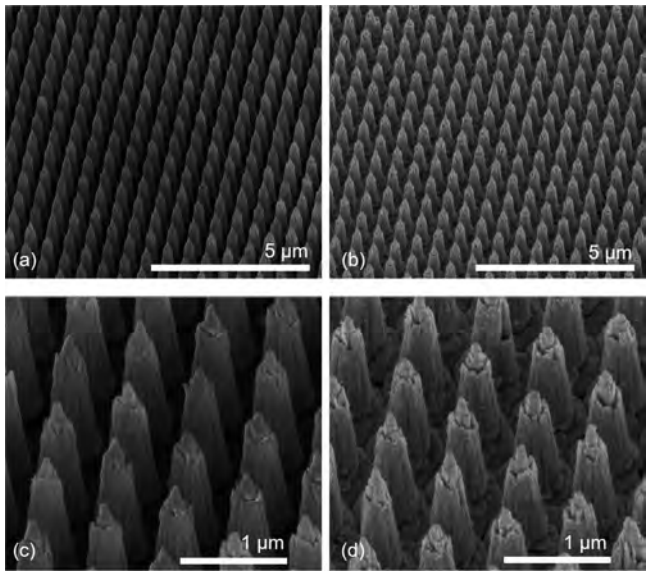

Figure 4. Scanning-electron micrographs of dry-etched TiO_2 nanocones on p^+n-Si substrates before (a,c) and after (b,d) electrodeposition of Ni.

energy-dispersive spectroscopy (EDS) mappings are included in Figure S6. The TiO_2 nanocones were ~2.3 μm tall and had base radii of ~250 nm. Discontinuities in the taper of the nanocones were evident, particularly near the vertex of each cone. The radii at the vertices of the nanocones were <50 nm. Figure 4b,d shows that the Ni predominantly deposited onto the Si surface in the spaces between the TiO_2 nanocones, as expected because the insulating 5−10 nm layer of SiO_2 beneath the base of the cones should prevent electrodeposition onto the TiO_2. The Ni layer was ~70 nm thick as estimated based on the charge passed during electrodeposition. The SEM image of a 50 nm thick Ni hole array fabricated via electron-beam patterning and dry etching is shown in Figure S7.

Figure S8 compares the real component of the complex refractive index measured by ellipsometry for the electron-beam-evaporated amorphous TiO_2 used to make nanocones in this work relative to the real component of the index of refraction of ideal rutile TiO_2 tabulated in standard reference data.[49] The real component of the refractive index for the electron-beam-evaporated TiO_2 was substantially lower (n = 2.05−2.3) than for the standard value (n = 2.7−3.3), presumably due to oxygen depletion during evaporation in conjunction with the amorphous phase of the TiO_2 film. Figure 5a shows the reflection, transmission, and absorption spectra calculated for TiO_2 nanocones with 50 nm Ni using the experimentally measured refractive index data for electron-beam-evaporated TiO_2, while Figure 5b shows the simulated transmitted photon flux along with the AM 1.5G spectrum. The estimated attainable photocurrent density calculated from these revised simulations for a Si solar cell covered with the TiO_2 nanocone array and Ni was $J_{ph,max}$ = 29.8 mA cm^{-2}, after correcting for losses due to reflection at the air/glass/water interfaces that are unavoidable in an electrochemical cell configuration. This estimated maximum photocurrent density ($J_{ph,max}$ = 29.8 mA cm^{-2}) was substantially lower than the current density that could be obtained with ideal TiO_2 ($J_{ph,max}$ = 36.5 mA cm^{-2}) but is still larger than the value expected for a bare, planar Si surface ($J_{ph,max}$ ~ 28 mA cm^{-2}).

DOI: 10.1021/acs.nanolett.9b04225
Nano Lett. 2020, 20, 502−508

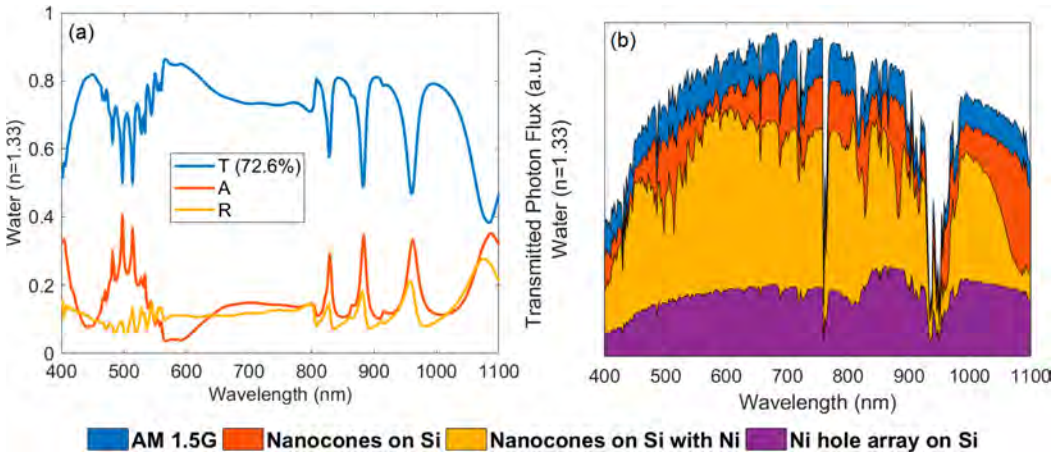

Figure 5. Transmission (T), absorption (A), and reflection (R) plots for Si with TiO_2 nanocones and 50 nm thick Ni calculated with evaporated TiO_2 refractive index data are shown in (a). (b) Area plot overlapped over the AM 1.5G spectrum for the three different cases, as shown in Figure 1, using the refractive index data for amorphous TiO_2 deposited by e-beam evaporation.

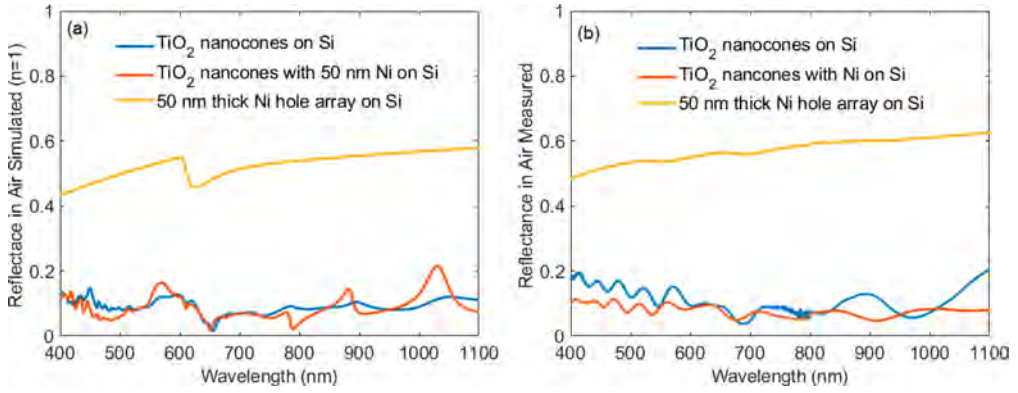

Figure 6. Reflection spectra (a) simulated and (b) measured for samples consisting of an array of TiO_2 nanocones on Si (blue), an array of TiO_2 nanocones with Ni on Si (red), an array of holes in a Ni layer on Si (yellow).

Figure 6 compares simulated and experimentally measured reflectance spectra for a TiO_2 nanocone array on Si, a TiO_2 nanocone array with Ni on Si, and for a 50 nm layer of Ni with an array of holes. The experimental and theoretical spectra are in good mutual agreement with certain differences readily ascribed to technical differences between the simulation and experimental conditions. For example, the simulations were performed using a coherent illumination source, whereas experimental measurements were not. Moreover, the simulations used smoothly tapering nanocones and a flat layer of Ni, whereas the samples did not have either smoothly tapering cones or a perfectly flat Ni layer (Figure 4).

Figure 7 shows the current density versus potential behavior in the dark and under 100 mW cm^{-2} of simulated AM1.5 illumination, respectively, while in contact with 1.0 M KOH(aq), for a photoanode made from a p^+n-Si substrate covered with an array of TiO_2 nanocones and a layer of Ni (Figure 4b,d). The light-limited photocurrent density, obtained by subtracting the current density measured in the dark at ~1 V versus the saturated calomel electrode (SCE) from the current density measured in the light at the same potential, was $\sim J_{ph,max}$ = 28 mA cm^{-2} and matched well with the value estimated ($J_{ph,max}$ = 29.8 mA cm^{-2}) from the simulations. The current density at the formal potential for water oxidation, $E^{\circ\prime}(O_2/H_2O)$ was 2−7 mA cm^{-2}. The observed light-limited photocurrent density was comparable

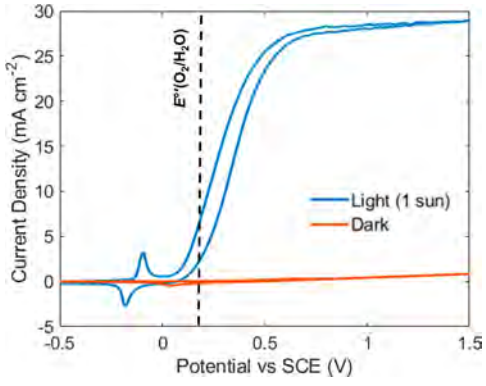

Figure 7. Current-density versus potential behavior in the dark and under 100 mW cm^{-2} of simulated AM1.5 solar illumination, respectively, for a p^+n-Si sample covered by an array of TiO_2 nanocones and 300 mC cm^{-2} of electrodeposited Ni while in contact with 1.0 M KOH(aq). The scan rate was 50 mV s^{-1}.

to the photocurrent density normally measured for a bare planar Si surface, consistent with the TiO_2 nanocones serving as antireflective structures that can couple to incoming light to enable transmission of light into the Si substrate even when ~54% of the Si surface was covered with ~70 nm of Ni.

Si photoanodes with a uniform 2 nm layer of Ni have been reported previously to exhibit a light-limited photocurrent

DOI: 10.1021/acs.nanolett.9b04225
Nano Lett. 2020, 20, 502−508

density of $J_{ph,max}$ ~ 55 mA cm^{-2} under ~2.25 Suns equivalent of illumination, whereas increasing the Ni thickness to 20 nm reduced $J_{ph,max}$ to ~32 mA cm^{-2}.[50] These results translate at 1 Sun intensity into $J_{ph,max}$ < 25 mA cm^{-2} for 2 nm Ni and <15 mA cm^{-2} with 20 nm Ni, whereas for comparison, the p$^+$n-Si photoanodes investigated herein exhibited $J_{ph,max}$ ~ 28 mA cm^{-2}. Although thick Ni catalysts are not required to lower the overpotential for water oxidation,[51] the use of thick electrocatalyst layers can minimize performance degradation associated with catalyst detachment.

A wide range of alternate approaches to efficient photoelectrode performance have been demonstrated, especially when active catalysts for the desired water-splitting half-reactions are used.[20] For example, p$^+$n-Si(111) photoanodes decorated with 15 nm thick Ni islands that covered 18% of the photoelectrode surface have demonstrated a light-limited current density of 20.4 mA cm^{-2}.[51] Modeling has shown that the optimal efficiency of a water-splitting system using a light-facing photocathode patterned with Pt islands covering 5% of the optical plane closely approaches that of a system using a photocathode patterned with a hypothetical transparent catalyst with the same activity as Pt.[52] Furthermore, photoanodes do not require reflective metallic catalyst coatings; indeed, p$^+$n-Si(100) photoanodes coated with 75 nm of sputtered NiO_x have been shown to be stable for 1200 h of continuous oxygen evolution in contact with 1.0 M KOH(aq) and exhibit a light-limited photocurrent density >30 mA cm^{-2}. The TiO_2 nanocone array structure can effectively optimize light transmission and catalysis simultaneously in a variety of possible materials systems and would be especially beneficial for chemical reactions that require very high mass loadings of catalysts, such as O_2 evolution or CO_2 reduction using earth-abundant electrocatalyst materials.

Dielectric nanocone arrays thus provide an additional option to a growing toolbox of strategies for directing broadband light around opaque top contacts to PV or PEC cells. The approach ought to be generally applicable for any combination of semiconductor and metal and in principle is scalable; however, arbitrary combinations of semiconductors and metals may not be compatible with electrodeposition of the metal onto the semiconductor as used in the fabrication process described herein. Furthermore, the fabrication process developed herein for a proof-of-concept experimental demonstration of a device that makes use of a TiO_2 nanocone array for light management was complex relative to other known options for light management, such as antireflective catalyst coatings or deposition of a controlled density and diameter of catalyst islands. The value of the dielectric nanocone approach to light management can be increased by developing a simplified fabrication process and by developing synthetic methods that yield TiO_2 nanocones with a refractive index that approaches the index for ideal TiO_2. Modeling and simulation efforts that compare attainable efficiencies for application-specific devices across relevant light-management strategies will prove valuable for identifying the strategies that are most promising for a given application.

■ ASSOCIATED CONTENT

Supporting Information

The Supporting Information is available free of charge at https://pubs.acs.org/doi/10.1021/acs.nanolett.9b04225.

Methods, simulated spectra of the TiO_2 film, simulated transmitted spectral photon flux, lateral distribution of transmitted light intensities, dimension variation effect on transmission, process flow diagram, EDS mapping of the TiO_2 nanocones with Ni sample, SEM image of the Ni hole array, and refractive index for TiO_2 (PDF)

■ AUTHOR INFORMATION

Corresponding Authors

*E-mail: haa@caltech.edu.
*E-mail: nslewis@caltech.edu.

ORCID

Wen-Hui Cheng: 0000-0003-3233-4606
Nathan S. Lewis: 0000-0001-5245-0538
Harry A. Atwater: 0000-0001-9435-0201

Author Contributions

#S.Y., E.V., and W.H.C. contributed equally.

Notes

The authors declare no competing financial interest.

■ ACKNOWLEDGMENTS

The fabrication and assessment of photoanodes for the oxygen-evolution reaction was supported through the Office of Science of the U.S. Department of Energy under Award No. DE-SC0004993 for the Joint Center for Artificial Photosynthesis and used facilities of the Kavli Nanoscience Institute at Caltech, a DOE Energy Innovation Hub; the development of simulations was supported by the National Science Foundation under award No. EEC-1041895.

■ REFERENCES

(1) Holman, Z.; Boccard, M. In *Photovoltaic Solar Energy: From Fundamentals to Applications*; John Wiley & Sons, Ltd.: Hoboken, NJ, 2016.
(2) Manzoor, S.; Yu, Z. J.; Ali, A.; Ali, W.; Bush, K. A.; Palmstrom, A. F.; Bent, S. F.; McGehee, M. D.; Holman, Z. C. *Sol. Energy Mater. Sol. Cells* **2017**, *173*, 59.
(3) Haug, F. J.; Ballif, C. *Energy Environ. Sci.* **2015**, *8*, 824.
(4) Schmid, M. *Semicond. Sci. Technol.* **2017**, *32*, 043003.
(5) Peer, A.; Biswas, R.; Park, J.-M.; Shinar, R.; Shinar, J. *Opt. Express* **2017**, *25*, 10704.
(6) Walter, M. G.; Warren, E. L.; McKone, J. R.; Boettcher, S. W.; Mi, Q.; Santori, E. A.; Lewis, N. S. *Chem. Rev.* **2010**, *110*, 6446.
(7) Hu, S.; Xiang, C.; Haussener, S.; Berger, A. D.; Lewis, N. S. *Energy Environ. Sci.* **2013**, *6*, 2984.
(8) Fountaine, K. T.; Lewerenz, H. J.; Atwater, H. A. *Nat. Commun.* **2016**, *7*, 13706.
(9) Raut, H. K.; Ganesh, V. A.; Nair, A. S.; Ramakrishna, S. *Energy Environ. Sci.* **2011**, *4*, 3779.
(10) Krč, J.; Smole, F.; Topič, M. *Prog. Photovoltaics* **2003**, *11*, 429.
(11) Campbell, P.; Green, M. A. *J. Appl. Phys.* **1987**, *62*, 243.
(12) Yablonovitch, E.; Cody, G. D. *IEEE Trans. Electron Devices* **1982**, *29*, 300.
(13) Cho, S. J.; An, T.; Lim, G. *Chem. Commun.* **2014**, *50*, 15710.
(14) Brongersma, M. L.; Cui, Y.; Fan, S. *Nat. Mater.* **2014**, *13*, 451.
(15) Mokkapati, S.; Catchpole, K. R. *J. Appl. Phys.* **2012**, *112*, 101101.
(16) Wilson, G. *AIP Conf. Proc.* **2016**, *1924*, 020003.
(17) Verlage, E.; Hu, S.; Liu, R.; Jones, R. J. R.; Sun, K.; Xiang, C.; Lewis, N. S.; Atwater, H. A. *Energy Environ. Sci.* **2015**, *8*, 3166.
(18) Zhou, X.; Liu, R.; Sun, K.; Chen, Y.; Verlage, E.; Francis, S. A.; Lewis, N. S.; Xiang, C. *ACS Energy Lett.* **2016**, *1*, 764.

DOI: 10.1021/acs.nanolett.9b04225
Nano Lett. 2020, 20, 502−508

(19) Cheng, W.-H.; Richter, M. H.; May, M. M.; Ohlmann, J.; Lackner, D.; Dimroth, F.; Hannappel, T.; Atwater, H. A.; Lewerenz, H.-J. *ACS Energy Lett.* **2018**, *3*, 1795.
(20) Sun, K.; Moreno-Hernandez, I. A.; Schmidt, W. C.; Zhou, X.; Crompton, J. C.; Liu, R.; Saadi, F. H.; Chen, Y.; Papadantonakis, K. M.; Lewis, N. S. *Energy Environ. Sci.* **2017**, *10*, 987.
(21) Yoshikawa, K.; Kawasaki, H.; Yoshida, W.; Irie, T.; Konishi, K.; Nakano, K.; Uto, T.; Adachi, D.; Kanematsu, M.; Uzu, H.; Yamamoto, K. *Nat. Energy* **2017**, *2*, 17032.
(22) Lammert, M. D.; Schwartz, R. J. *IEEE Trans. Electron Devices* **1977**, *24*, 337.
(23) Spitzer, M. B.; Fan, J. C. C. *Sol. Cells* **1990**, *29*, 183.
(24) Garnett, E.; Yang, P. D. *Nano Lett.* **2010**, *10*, 1082.
(25) Tian, B. Z.; Zheng, X. L.; Kempa, T. J.; Fang, Y.; Yu, N. F.; Yu, G. H.; Huang, J. L.; Lieber, C. M. *Nature* **2007**, *449*, 885.
(26) Wallentin, J.; Anttu, N.; Asoli, D.; Huffman, M.; Aberg, I.; Magnusson, M. H.; Siefer, G.; Fuss-Kailuweit, P.; Dimroth, F.; Witzigmann, B.; Xu, H. Q.; Samuelson, L.; Deppert, K.; Borgstrom, M. T. *Science* **2013**, *339*, 1057.
(27) Mavrokefalos, A.; Han, S. E.; Yerci, S.; Branham, M. S.; Chen, G. *Nano Lett.* **2012**, *12*, 2792.
(28) Zhu, J.; Hsu, C. M.; Yu, Z. F.; Fan, S. H.; Cui, Y. *Nano Lett.* **2010**, *10*, 1979.
(29) Yao, Y.; Yao, J.; Narasimhan, V. K.; Ruan, Z. C.; Xie, C.; Fan, S. H.; Cui, Y. *Nat. Commun.* **2012**, *3*, 664.
(30) Kapadia, R.; Fan, Z. Y.; Takei, K.; Javey, A. *Nano Energy* **2012**, *1*, 132.
(31) Narasimhan, V. K.; Hymel, T. M.; Lai, R. A.; Cui, Y. *ACS Nano* **2015**, *9*, 10590.
(32) Jeong, S.; Garnett, E. C.; Wang, S.; Yu, Z. G.; Fan, S. H.; Brongersma, M. L.; McGehee, M. D.; Cui, Y. *Nano Lett.* **2012**, *12*, 2971.
(33) Yalamanchili, S.; Emmer, H. S.; Fountaine, K. T.; Chen, C. T.; Lewis, N. S.; Atwater, H. A. *ACS Photonics* **2016**, *3*, 1854.
(34) Fountaine, K. T.; Cheng, W.-H.; Bukowsky, C. R.; Atwater, H. A. *ACS Photonics* **2016**, *3*, 1826.
(35) Fountaine, K. T.; Kendall, C. G.; Atwater, H. A. *Opt. Express* **2014**, *22*, A930.
(36) Grandidier, J.; Callahan, D. M.; Munday, J. N.; Atwater, H. A. *Adv. Mater.* **2011**, *23*, 1272.
(37) Choy, J. T.; Bradley, J. D. B.; Deotare, P. B.; Burgess, I. B.; Evans, C. C.; Mazur, E.; Lončar, M. *Opt. Lett.* **2012**, *37*, 539.
(38) Evans, C. C.; Liu, C.; Suntivich, J. *Opt. Express* **2015**, *23*, 11160.
(39) Evans, C. C.; Shtyrkova, K.; Bradley, J. D. B.; Reshef, O.; Ippen, E.; Mazur, E. *Opt. Express* **2013**, *21*, 18582.
(40) Evans, C. C.; Shtyrkova, K.; Reshef, O.; Moebius, M.; Bradley, J. D. B.; Griesse-Nascimento, S.; Ippen, E.; Mazur, E. *Opt. Express* **2015**, *23*, 7832.
(41) Guan, X.; Hu, H.; Oxenløwe, L. K.; Frandsen, L. H. *Opt. Express* **2018**, *26*, 1055.
(42) Bradley, J. D. B.; Evans, C. C.; Choy, J. T.; Reshef, O.; Deotare, P. B.; Parsy, F.; Phillips, K. C.; Lončar, M.; Mazur, E. *Opt. Express* **2012**, *20*, 23821.
(43) Sun, K.; Kuang, Y.; Verlage, E.; Brunschwig, B. S.; Tu, C. W.; Lewis, N. S. *Adv. Energy Mater.* **2015**, *5*, 1402276.
(44) Hu, S.; Shaner, M. R.; Beardslee, J. A.; Lichterman, M.; Brunschwig, B. S.; Lewis, N. S. *Science* **2014**, *344*, 1005.
(45) Lichterman, M. F.; Carim, A. I.; McDowell, M. T.; Hu, S.; Gray, H. B.; Brunschwig, B. S.; Lewis, N. S. *Energy Environ. Sci.* **2014**, *7*, 3334.
(46) McDowell, M. T.; Lichterman, M. F.; Carim, A. I.; Liu, R.; Hu, S.; Brunschwig, B. S.; Lewis, N. S. *ACS Appl. Mater. Interfaces* **2015**, *7*, 15189.
(47) McDowell, M. T.; Lichterman, M. F.; Spurgeon, J. M.; Hu, S.; Sharp, I. D.; Brunschwig, B. S.; Lewis, N. S. *J. Phys. Chem. C* **2014**, *118*, 19618.
(48) Shaner, M. R.; Hu, S.; Sun, K.; Lewis, N. S. *Energy Environ. Sci.* **2015**, *8*, 203.
(49) Siklitsky, V. Available at http://www.ioffe.rssi.ru/SVA/NSM, 2001 (accessed December 2018).
(50) Kenney, M. J.; Gong, M.; Li, Y.; Wu, J. Z.; Feng, J.; Lanza, M.; Dai, H. *Science* **2013**, *342*, 836.
(51) Sun, K.; Ritzert, N. L.; John, J.; Tan, H.; Hale, W. G.; Jiang, J.; Moreno-Hernandez, I.; Papadantonakis, K. M.; Moffat, T. P.; Brunschwig, B. S.; Lewis, N. S. *Sustainable Energy Fuels* **2018**, *2*, 983.
(52) Chen, Y.; Sun, K.; Audesirk, H.; Xiang, C.; Lewis, N. S. *Energy Environ. Sci.* **2015**, *8*, 1736.

DOI: 10.1021/acs.nanolett.9b04225
Nano Lett. 2020, 20, 502−508